PHOTOACOUSTIC SENSING AND IMAGING

A Record of Study

by

SEAN ZACHARY ROBERSON

Submitted to the Department of Mathematics of
The University of Texas at San Antonio
in partial fulfillment of the requirements for the degree of

MASTER OF SCIENCE

Supervising Professor,	Dmitry Gohkman
Supervising Researchers,	Randolph Glickman
	Saher Maswadi
Graduate Advisor of Record,	Duy Nguyen Vu Hoang
Head of Department,	Juan B. Gutiérrez

December 2023

Major Subject: Mathematics

ABSTRACT

Among many imaging techniques available in medicine and industry, photoacoustic methods provide a minimally invasive manner in which to acquire data. Existing literature describes imaging via radial detectors, as in traditional tomography. An alternative is to image via averaging over lines. A line detector approach can be used to find defects and phantoms that are small in scale. This paper outlines the physical and mathematical foundations of photoacoustic imaging and summarizes experiments conducted as part of an internship project with Echolase, Inc., a startup in San Antonio, Texas.

DEDICATION

To my mother Denise, my stepfather Matthew, and my late father David, for always believing in my abilities.

ACKNOWLEDGMENTS

There are so many people I would like to thank - if I were to include all their names, this document would be much longer than needed.

First and foremost, I would like to thank Dr. Duy Nguyen Vu Hoang, the advisor of record for the Applied-Industrial Mathematics program at UTSA. Not only did he encourage me to seek out opportunities in research and guide me through the program, his connections were able to allow me to begin working at Echolase, Inc.

Of course, I could not have begun the project and made substantial progress without the guidance of Dr. Randolph Glickman and Dr. Saher Maswadi. I came into this project knowing very little about photoacoustics, but the motivation to seek out knowledge and experiment gave me a basic understanding of the field. Their support has given me valuable experience in a short-term research setting.

There are two more faculty members I wish to acknowledge for their support in my academic pursuit. Dr. Walter Richardson has provided numerous insights on the importance of data in modern scientific computing, and through his courses in mathematical modeling and numerical linear algebra, I find that I am better equipped to tackle similar projects as this one. His insights into the mathematics behind the physical principles has allowed me to dig deep into my own work and provide results related to my goals.

I would also like to thank Dr. Juan Gutiérrez, chair of the mathematics department, for giving my academic career at UTSA an incredible start. Without his encouragement, I would not have found myself completing this degree after a hiatus and transfer to a new program. He has given me the confidence to apply myself in a future industry, government, or research position as an individual aware of the multidisciplinary nature of mathematics.

Friendship is a powerful support system. Much of the encouragement in my short time at UTSA has come from Christopher Ayo, a colleague and friend whose positive mindset kept me focused on my goals. In addition to the many friends I have gained through my academic career

- including those I met on campus and worked with in and out of classrooms - and those in local music scenes (and beyond - here's to you, ska fans), I want to express my gratitude to some of my friends from my time in College Station - Desiree Corona, Cory Hill, Amanda Kalinec-Corona, Krystn Locke, Mike Pawlus, and Laura Waller. Their support and encouragement has kept me going, even in the toughest times. Thank you for the many adventures filled with songs, joy, and laughter.

No list of thanks would be complete without mentioning my family. I am forever thankful for my mother and stepfather, Denise and Matthew Ginther, for continuing to push me to succeed even in the eyes of adversity. This has been a long journey, and I am so blessed to come to the end with more skills. Thank you for the love and encouragement through the stressful times. Your love gives me the fuel to strive for knowledge and success.

CONTRIBUTORS AND FUNDING SOURCES

Contributors

This work was supported by Professor Dmitry Gohkman [supervising professor] and Professor Duy Nguyen Vu Hoang [advisor of record for Applied-Industrial Mathematics program]. Work conducted at Echolase, Inc. was supported by Drs. Randolph Glickman and Saher Maswadi.

Analyses were conducted with the insight of Drs. Glickman and Maswadi. All other work was conducted independently by the student.

Funding Sources

Graduate study was supported by a teaching assistantship from the University of Texas at San Antonio Department of Mathematics. Funding for the internship project was provided by Echolase, Inc.

TABLE OF CONTENTS

Page

LIST OF FIGURES

FIGURE Page

1. INTRODUCTION[1]

1.1 Principles of Photoacoustics

Lasers have many uses in modern medicine. A common use is in corrective eye surgery, which removes small parts of the cornea to correct astigmatism. Another use is in the imaging of various biological tissues. Through photoacoustic imaging, high resolution images can be created to seek defects in skin, tumors, blood vessels, and vital organs. Echolase, a medical startup based in San Antonio, Texas, has designed a photoacoustic imaging technology to specifically detect ultrasound pulses via a probe beam deflection technique (PBDT). This chapter will provide a background on the principles of photoacoustics and outline the main goals of the project.

1.2 Approach

The primary principle of photoacoustics stems from the absorption of light pulses in the target material. When light is directed towards a tissue sample, the irradiated area absorbs the light, is heated, and undergoes a thermoelastic expansion-contraction cycle, thus creating a pressure wave that travels through the sample material and potentially into a surrounding medium, such as a tank of water. The extent and amplitude of this pressure wave can be measured by observing pressure transients in that medium. With short laser pulses in the range of 10^{-9} seconds, the frequencies of these pressure waves lie in the ultrasound frequency range of 1 and 50 MHz. These ultrasonic waves can then be used to construct a desired image of the tissue to examine any defects. Depending on the duration of the pulse, one can observe various photomechanical, photothermal, and photochemical changes in the desired material to be imaged. Photoacoustic methods have the advantage of being safe and non-invasive, provided the laser exposures are below the limits defined in the ANSI safety standards. This allows for low-energy radiation compared to CT scans and nuclear imaging. The resulting temperature changes induced by the laser are small, approximately a fraction of a degree. An extended introductory treatment can be found in [9] and [5]. A schematic

[1]This chapter is adapted from the initial research proposal.

with the design of Echolase's system is found in [10], with a discussion on preliminary findings. Also of interest is how the laser interacts with various tissues, such as skin or muscle. An overview of these interactions along with some experimental results is found in [8], with explanations of the scattering properties of lasers at different wavelengths.

1.3 Project Goals

For the specific project with Echolase, the research will use test materials to examine the effectiveness of the photoacoustic imaging techniques. To obtain preliminary results, metal test parts with phantom defects (such as holes, cuts, and other imperfections) were used as subjects in the image reconstruction process. The goal is to use the PBDT detector to provide sharper responses with little interference to create high resolution images as compared to conventional ultrasound imaging methods. To attain this goal, routines were created using the LabView software suite to control the delivery of the laser to the target material, perform scans of the phantom metals, and create two-dimensional images.

The project will also serve as a bridge to the applications of mathematics in the research workplace. The goal is to apply skills learned in upper division and graduate courses to solve a research question while collecting information from various sources and creating a significant result. Such a project can serve as a guide for future graduate students in the Applied-Industrial Mathematics program and in other disciplines at the university.

2. MATHEMATICAL FRAMEWORK OF PHOTOACOUSTIC IMAGING

In this chapter, we discuss the mathematical foundations of photoacoustic imaging by relating it to existing techniques, as well as recent developments in the field. We also discuss approaches to image reconstruction using machine learning frameworks. While we mainly focus on the mathematics in this paper, detailed discussions on the physical framework can be found in, e.g., papers by Glickman [5], Li [9], and Maswadi [10].

2.1 The Forward Problem

The forward problem in photoacoustic imaging, as demonstrated in the papers by Paltauf et al. [11] and Haltmeier et al. [6], is given by the following two-dimensional wave equation with the unknown acoustic pressure p:

$$\begin{cases} \dfrac{\partial^2 p}{\partial t^2} - \Delta p = 0 \\ p(x,y,0) = p_0(x,y) \\ p_t(x,y,0) = 0 \end{cases} \tag{2.1}$$

where the initial pressure profile $p_0(x,y)$ is the image to be reconstructed. We shall note that although the formulation given in [11] invokes the nonhomogenous form with respect to the velocity potential, the above representation of the partial differential equation is equivalent by Duhamel's principle, as given in Evans' text [3]. This equation also rescales the time units, so that the physical constants relating to the density of material, speed of sound, and specific heat of the material are accounted for. The solution is found using the Kirchhoff formula

$$p(x,y,t) = \frac{1}{4\pi c^2 t}\,\frac{\partial}{\partial t} \int\limits_{|r-r'|=ct} p_0(r')\,dS \tag{2.2}$$

where $r = (x,y)$, $r' = (x',y')$, and dS is the surface measure on the sphere (a full treatment is given in Evans [3] and [14], referred to as the method of spherical means). As the experiment to be

considered in chapter 3 is based on a line detector, we reduce the traditional three-dimensional problem to one in two dimensions where the signals $q(x,y,t)$ received are computed by the integral

$$q(x,y,t) = \int_{-\infty}^{\infty} p(x,y,z,t)\, dz. \tag{2.3}$$

That is, we shall assume that the lines are infinitely long in the z-direction, though a practical application can assume that the function p is compactly supported on some interval $[-L,L]$.

After inserting equation 2.3 into the integral in equation 2.2, we obtain, after an exchange of integrals,

$$q(x,y,t) = \frac{1}{2\pi c}\,\frac{\partial}{\partial t} \int_{|r-r'|<ct} \frac{q_0(r')}{\sqrt{c^2t^2 - |r-r'|^2}}\, dA' \tag{2.4}$$

where dA' is the area measure $dx'dy'$, and the function q_0 is the initial signal, similar to that computed in equation 2.3. We remark that solving for the unknown $p_0(x,y,t)$ will give $q_0(x,y,t)$, though there are numerous approaches to this inverse problem.

2.2 Image Reconstruction

We give an overview of some of the methods of image reconstruction described in the literature. While most approaches in medical and material imaging refer to three-dimensional reconstruction, we restrict the descriptions here to two dimensions.

2.2.1 Frequency Domain Approach via Fourier Transforms

Most of the literature refers to a frequency domain approach for three-dimensional image reconstruction, but the method desired for the applications at Echolase is a two-dimensional reconstruction from lines. By considering the Fourier transform of the functions q and q_0 in equation 2.4, we obtain the transformed representation of the initial source

$$Q_0(k_x,k_y) = \frac{2ck_y}{\boldsymbol{\omega}\cdot \operatorname{sgn}(k_y)} Q(k_x, c\boldsymbol{\omega}\cdot \operatorname{sgn}(k_y)) \tag{2.5}$$

where $\omega = \sqrt{k_x^2 + k_y^2}$ and sgn denotes the signum function. After inversion, this gives an exact reconstruction of the original source data q_0, but only if the data are acquired along an infinite line. For many applications, however, the line is considered to be finite length (owing to the previously assumed compact support), so reconstructing an image in this fashion is prone to have artificats. Paltauf suggests improving the reconstruction by scanning along a line orthogonal to the original position. This provides a duality in the scans - information missing from the first is found in the second, and conversely. The sum of the reconstructed images is an adequate approximation of the source [11].

2.2.2 Time Domain Approach via Back-Projection

Another common reconstruction method is back-projection, which is done in the time domain. One approach to this is mentioned in the texts by Epstein [2] and Feeman [4] using the Radon transform. This transform averages over parallel lines that correspond to slices of an object. For a continuous function with compact support, the integral along the line $l_{t,\omega}$ represented by the inner product

$$\langle x, \omega \rangle = x_1 \omega_1 + x_2 \omega_2 = t$$

where $\omega \in S^1$ is a unit vector $(\cos\theta, \sin\theta)$, the Radon transform of f is the function

$$\mathscr{R}f(t, \omega) = \int_{-\infty}^{\infty} f(t\omega + s\hat{\omega})\, ds \tag{2.6}$$

where the vector $\hat{\omega}$ is the unit vector orthogonal to ω. A possible guess for the inverse transform is given by the back-projection integral

$$\mathscr{B}f(x) = \tilde{f}(x) = \frac{1}{\pi} \int_0^{\pi} \mathscr{R}f(\langle x, \omega(\theta) \rangle, \theta)\, d\theta \tag{2.7}$$

which, while fitting the usual idea for an inverse, does not fully reconstruct the image. Instead, as this integral appears similar to mean-value formulas, the back-projection image is smoothed, mak-

ing some features blurry as a result of averaging. This can pose a problem for phantom detection in materials and tissue. This can be remedied, however, by introducing a filtered approach via the two-dimensional Fourier transform.

In the filtered back-projection formula, we use the conventions for the forward and inverse two-dimensional Fourier transforms: the forward transform operator $\mathscr{F}$ is defined by

$$\hat{f}(\xi) = \mathscr{F} f(\xi) = \iint_{\mathbb{R}^2} f(x) e^{-i\langle \xi, x \rangle} \, dx \tag{2.8}$$

and its inverse $\mathscr{F}^{-1}$ is

$$\mathscr{F}^{-1} \hat{f}(x) = \frac{1}{4\pi^2} \iint_{\mathbb{R}^2} \hat{f}(\xi) e^{i\langle x, \xi \rangle} \, d\xi. \tag{2.9}$$

Before stating the filtered back-projection result, we state a relationship between the Radon and Fourier transforms known as the central slice theorem.

Theorem 2.1 (Central Slice Theorem)**.** *Denote by $\mathscr{D}$ the natural domain of the Radon transform operator $\mathscr{R}$ as*

$$\mathscr{D} = \{ f : f\big|_{l_{t,\omega}} \in L^1(\mathbb{R}) \}.$$

Suppose $f \in \mathscr{D}$. Then for each $r \in \mathbb{R}$ and unit vector ω,

$$\hat{f}(r\omega) = \int_{\mathbb{R}} \mathscr{R} f(t, \omega) e^{-itr} \, dt.$$

Proof. By using the definition of the Radon transform as seen in equation 2.6, we have

$$\int_{\mathbb{R}} \mathscr{R} f(t, \omega) e^{-itr} \, dt = \iint_{\mathbb{R}^2} f(t\omega + s\hat{\omega}) e^{-itr} \, ds \, dt.$$

Now as $f \in \mathscr{D}$, the integral on the right side converges absolutely. Let $x = t\omega + s\hat{\omega}$. Then the new

measure dx is computed as

$$\begin{aligned} dx &= \begin{vmatrix} \cos\theta & -\sin\theta \\ \sin\theta & \cos\theta \end{vmatrix} ds\, dt \\ &= ds\, dt. \end{aligned}$$

Now because the parameter t is defined as the inner product $\langle x, \omega \rangle$, the integral can be written as

$$\begin{aligned} \iint_{\mathbb{R}^2} f(t\omega + s\hat{\omega}) e^{-itr}\, ds\, dt &= \iint_{\mathbb{R}^2} f(x) e^{-itr}\, dx \\ &= \iint_{\mathbb{R}^2} f(x) e^{-ir\langle x,\omega\rangle}\, dx \\ &= \iint_{\mathbb{R}^2} f(x) e^{-i\langle x, r\omega\rangle}\, dx \\ &= \hat{f}(r\omega) \end{aligned}$$

as desired. □

We remark that this reduces the computation of a two-dimensional Fourier transform as one in the single variable $r\omega$, which is called the affine parameter. This representation also relates to a polar coordinate transformation, and so integration along lines amounts to integrating around concentric circles through a diameter. This observation does allow for a Parseval-type formula for the Radon transform.

Theorem 2.2 (Parseval's Theorem for the Radon Transform)**.** *Suppose $f \in \mathscr{D} \cap L^2(\mathbb{R})$. Then*

$$\iint_{\mathbb{R}^2} |f(x)|^2\, dx = \frac{1}{4\pi^2} \int_0^{\pi} \int_{\mathbb{R}} |\widetilde{\mathscr{R}f}(r,\omega)|^2 |r|\, dr\, d\omega$$

where $\widetilde{\mathscr{R}f}(r,\omega) = \hat{f}(r\omega)$.

Proof. The proof uses the central slice theorem and relies on the fact that the Radon transform is

an even function. Otherwise, f must be approximated by a sequence of $L^1(\mathbb{R})$ functions. See [2, p. 186-187] for a full treatment. □

The central slice theorem is the vehicle to prove the inversion formula for the Radon transform.

Theorem 2.3 (Radon Inversion Formula)**.** *Suppose $f \in \mathscr{D} \cap L^1(\mathbb{R})$ and $\hat{f} \in L^1(\mathbb{R}^2)$. Then*

$$f(x) = \frac{1}{4\pi^2} \int_0^{\pi} \int_{\mathbb{R}} e^{ir\langle x,\omega\rangle} \widetilde{\mathscr{R}f}(r,\omega)|r| \, dr \, d\omega.$$

Proof. Use the Fourier inversion formula to express the integral representation of $\mathscr{F}^{-1}\hat{f}$ in polar coordinates and write

$$\begin{aligned} f(x) &= \frac{1}{4\pi^2} \iint_{\mathbb{R}^2} \hat{f}(\xi) e^{i\langle x,\xi\rangle} \, d\xi \\ &= \frac{1}{4\pi^2} \int_0^{2\pi} \int_0^{\infty} e^{ir\langle x,\omega\rangle} \hat{f}(r\omega) \, r \, dr \, d\omega. \end{aligned}$$

The inner integral can be extended to all of $\mathbb{R}$ by the fact that $\mathscr{R}f$ is even, and so too is its Fourier transform. So, by the symmetry and the central slice theorem,

$$\begin{aligned} \frac{1}{4\pi^2} \int_0^{2\pi} \int_0^{\infty} e^{ir\langle x,\omega\rangle} \hat{f}(r\omega) \, r \, dr \, d\omega &= \frac{1}{4\pi^2} \int_0^{2\pi} \int_{-\infty}^{\infty} \frac{1}{2} e^{ir\langle x,\omega\rangle} \hat{f}(r\omega) \, |r| \, dr \, d\omega \\ &= \frac{1}{4\pi^2} \int_0^{2\pi} \int_{-\infty}^{\infty} \frac{1}{2} e^{ir\langle x,\omega\rangle} \widetilde{\mathscr{R}f} \, |r| \, dr \, d\omega \\ &= \frac{1}{4\pi^2} \int_0^{\pi} \int_{-\infty}^{\infty} e^{ir\langle x,\omega\rangle} \widetilde{\mathscr{R}f} \, |r| \, dr \, d\omega \end{aligned}$$

as desired. □

An alternative statement of this inversion formula can be found in the text by Debnath [1, p. 556], although the integral is taken over a unit circle, and the constant at the front of the integral

includes a minus sign. The presentation in that text is given after a discussion of the Hilbert transform, compared to those in Epstein [2] and Feeman [4].

The second to last line in the proof gives a representation of the source function f using the Fourier transform. If we let $\mathscr{B}$ be the back-projection operator defined in equation 2.7, then we may write

$$f(x) = \frac{1}{2}\mathscr{B}\left(\mathscr{F}^{-1}\left(|r|\mathscr{F}\right)\right)(x). \tag{2.10}$$

This can also be represented in terms of the Hilbert transform - see Feeman [4, p. 75].

2.2.3 Other Image Reconstruction Approaches

Other approaches to image reconstruction of photoacoustic signals include machine learning frameworks. The imaging problem as stated in the paper by Haltmeier et al. [6] as finding the image $X \in \mathbb{R}^{d\times d}$ such that

$$Y = \mathbb{A}(X) + \xi \tag{2.11}$$

where $Y \in \mathbb{R}^{M\times N}$ is the given data (say, measurements from a sensor), and ξ is a matrix of noise. The operator $\mathbb{A}$ is referred to as the imaging operator, and moves forward in time. The image reconstruction is done here using a convolutional neural network with L layers, with each layer the composition of a linear mapping W_i of weights and a nonlinear map σ_i applied to each entry. Combined with a discretized back-projection operator, their proposed implementations use a network for image segmentation, which is useful for edge detection of phantoms in images. Using this on a machine without a dedicated GPU may be computationally expensive, and achieving high resolution may be impossible without additional hardware or access to cloud computing resources.

Paltauf et al. [11] also suggests iterative reconstruction techniques. In particular, they refer to Kaczmarz-type methods, but their discussion refers to spherical means. However, they modify the approach to include a relaxation parameter that does not update if the residual at a certain stage is below a specified bound. This is different than the usual Kaczmarz method, which is based on a series of projections onto lines [2, Ch. 13.2]. The approach is constructed similarly to gradient descent methods. Given a family of I hyperplanes in $\mathbb{R}^J$, we wish to solve the system of linear

equations $\langle r_i, x\rangle = p_i$, where $i = 1, \ldots, I$ and $r_i \in \mathbb{R}^J$. The algorithm is based on the recursion with a given guess $x^{(0)}$:

$$x^{(k,n+1)} = x^{(k,n)} - \frac{\langle x^{(k,n)}, r_{n+1}\rangle - p_{n+1}}{\langle r_{n+1}, r_{n+1}\rangle} r_{n+1} \tag{2.12}$$

If $n = I - 1$ then $x^{(k,n)} = x^{(k+1)}$. Of course, there are variants to this similar to classical gradient descent, such as a control on the step size and a randomized approach. The randomized algorithm selects a row at each stage and projects onto another hyperplane. The sampling method is done proportional to the norm of the coefficient vector in the selected row. The convergence of this method is slow and depends on the condition number of the system matrix A. If x^* is the solution to $Ax = b$, then the mean-squared error at stage k of the randomized Kaczmarz algorithm satisfies the bound

$$E\left(||x_k - x^*||^2\right) \leq \left(1 - \frac{1}{c^2}\right)^k ||x_0 - x^*||^2$$

where c is the condition number of A. If c is very large, then this convergence is slow compared to usual gradient descent methods. This bound was proved by Strohmer and Vershynin [13, p. 364-365].

3. EXPERIMENTAL INVESTIGATIONS IN PHOTOACOUSTIC WAVE GENERATION[2]

This chapter outlines the preliminary experiments conducted in measuring the profile of a photoacoustic pulse in our setup. Some of the design is adapted from [10], albeit with a different experimental setup.

3.1 Experiment Objective and Setup

The aim of the experiment is to measure the acoustic pressure wave generated by the laser. In order to accurately measure this response, we first obtain the shape of the beam by a knife-edge test. After this profile is attained, a detector is moved within a tank of water to measure the acoustic response from the laser striking a target placed inside the tank. The target is an absorber consisting of a thin black plastic (approximately 0.5 mm thick) in a holder - see figure 3.1.

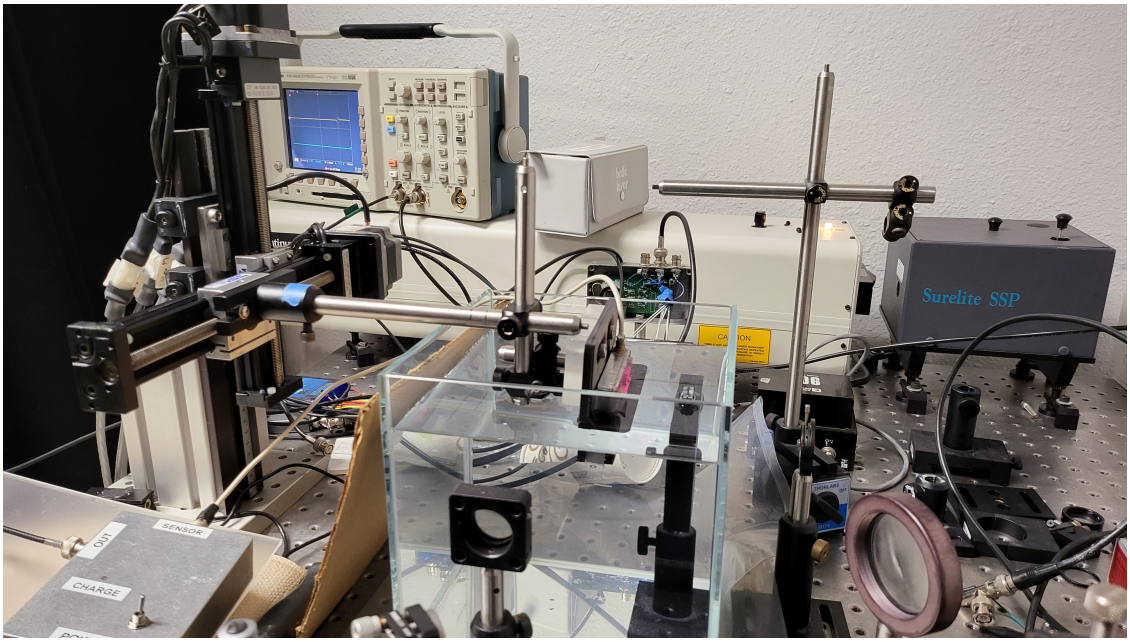

Figure 3.1: The experimental setup for measuring the acoustic field. The detector is currently placed in the center of the tank (see figure 3.2 for a detailed photograph of the detector). At the right side of the tank is the submerged target.

[2]Portions of this chapter are adapted from a submitted midterm progress report.

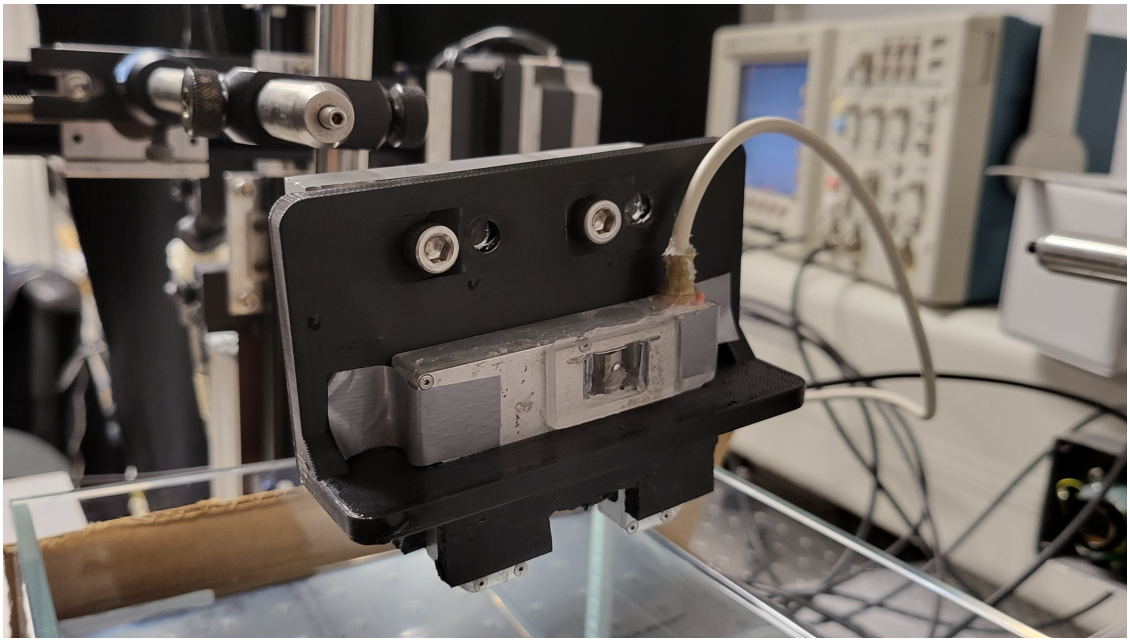

Figure 3.2: A closeup of the detector used in the experiment.

3.2 Beam Profile via a Knife-Edge Test

Before we can image our test materials using a photoacoustic model, we must first determine the shape of our laser beam so that the responses can be accurately measured. To do this, we conduct a knife-edge test to construct a cross-sectional profile of the beam.

To conduct the test, we first mount a razor blade on a translation stage attached to a micrometer. The micrometer allows the blade to move laterally with precision up to 0.001in. When the laser is active and passes near the razor, some of the light is blocked. We incrementally move the razor and measure the amplitude of the signal collected by a photodiode which is connected to an oscilloscope. Measurements were obtained from when the beam was fully exposed to the diode to when it was blocked by the razor.

Measurements were collected over two sessions. In the first session, one reading was taken from 97 lateral positions along the translation stage. Measurements were taken at intervals of 0.005 in, with some readings being taken at intervals of 0.025 in. The fit obtained from this session did not provide satisfactory results, and the test was conducted again, but with finer divisions

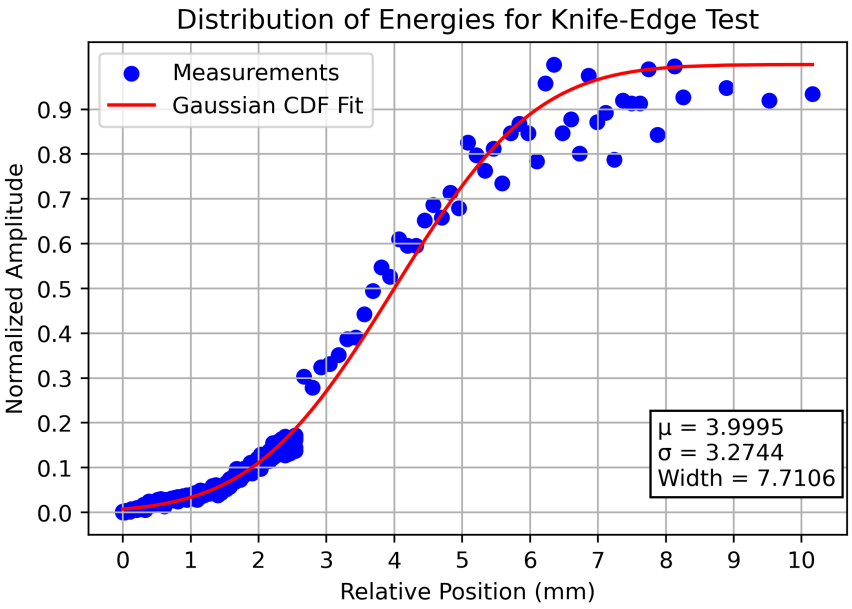

Figure 3.3: A distribution of energies at various positions as measured by the knife-edge test. Amplitudes have been normalized.

between successive readings. The second session used intervals ranging from 0.001 in to 0.005 in between readings, and four measurements were taken at each recorded position. This produced a total of 280 measurements, and combining with some readings from the previous session, a total of 327 data points were used. The amplitudes read from the oscilloscope were then normalized, and after deleting an outlier, the data were plotted, and they appear to follow a sigmoid curve shape. See figure 3.3. The method of determining the shape of the beam is done in the similar fashion as in [10], except that the minimum energy is normalized to a measurement of 0 as opposed to 1.

A simple non-linear least squares regression was conducted using the Gaussian cumulative distribution function

$$F(x;\mu,\sigma) = \frac{1}{2}\left(1+\operatorname{erf}\left(\frac{x-\mu}{\sigma\sqrt{2}}\right)\right)$$

where erf is the error function

$$\operatorname{erf}(x) = \frac{2}{\sqrt{\pi}}\int_0^x e^{-z^2}\,dz.$$

From this, we found that the data approximately followed a Gaussian distribution with mean $\hat{\mu} =$

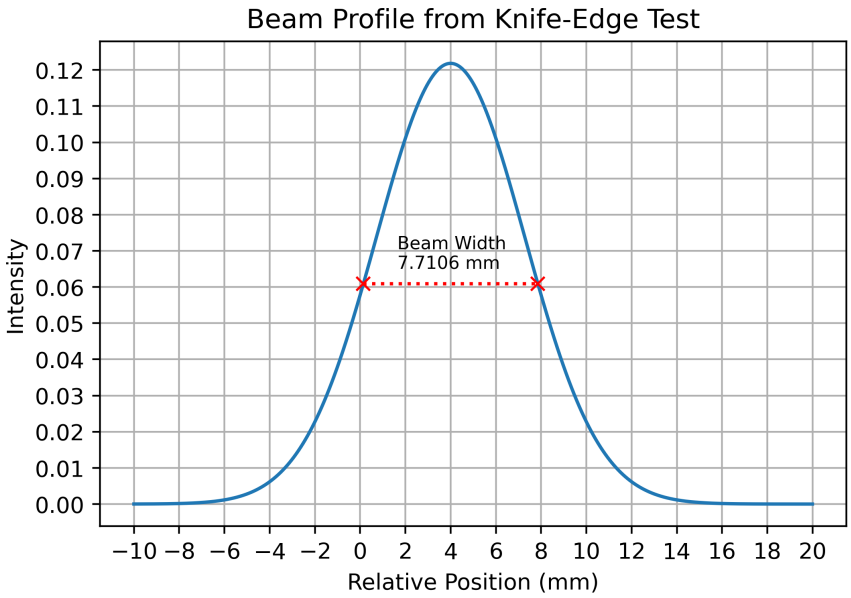

Figure 3.4: Cross section of estimated beam profile as measured in figure 3.3. The beam width here is calculated by the Full Width at Half Maximum (FWHM).

3.9995 and standard deviation $\hat{\sigma} = 3.2744$. With this information, we can estimate the beam's width, which is quantified by the full width at half-maximum (FWHM). This measurement is obtained by determining the width of the beam when the energy density is at half its maximum. Note that the right tail of the energy distribution shows some artifacts of light scattering, which is a result of the experimental setup. We also remark that the shape of the beam is approximately elliptical, with the scan performed along its major axis. Verifying this shape is considered in future work.

Another measure of beam width that is commonly used is the $1/e^2$ measurement, which is the distance across the beam cross-section where the intensity takes the value $1/e^2$, where e is the Euler constant. The FWHM and $1/e^2$ measures are related by

$$2w = 1.699 \cdot \text{FWHM}$$

where $2w$ is the $1/e^2$ width [7]. Note that in figure 3.4, the FWHM width is reported.

3.3 Ultrasound Wave Profile

The next preliminary reading to obtain is a profile of the ultrasound wave generated by the laser after it strikes a target submerged in distilled water. A detector was mounted onto a two-axis translation stage which is controlled by a pair of motors via computer commands. Initially, the detector was placed approximately 5 cm from the target, and an initial raster scan was performed. The scan measured the initial acoustic pressure responses from the target to the detector on a 44×44 grid measuring 2.794 cm $\times$ 2.794 cm in area.

Each scan was captured in a 100 μs window. For positions where a clear signal was obtained (i.e., noise from the detector being too far away from the beam was absent), we observe the position of the initial photoacoustic response and measure the total peak-to-peak amplitude. At present, a scan along the major axis of the elliptical beam was observed. This profile, along with the scan along the minor axis, will be used to determine the approximate shape of the pressure wave. The plot in figure 3.5 shows the approximate shape of this pressure wave measured along its major axis. Observe that again the wave follows an approximate Gaussian shape at each slice. We expect a similar profile along the minor axis, though the width may be shorter along that direction.

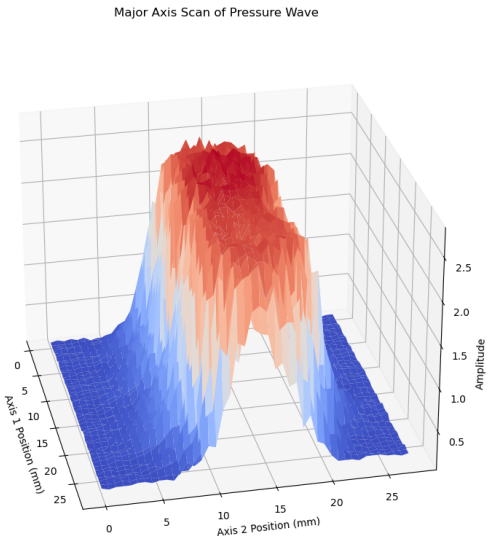

Figure 3.5: A surface plot of the ultrasound pressure wave, measured along its long axis.

4. SUMMARY AND CONCLUSIONS

After analyzing the beam profile and shape of the acoustic field, we determine the shape of an acrylic lens to focus the field. The focusing of the field is to enable a future imaging application to have higher resolution than a previous experiment. This chapter summarizes the results of the scan experiments, dimensions of the lens, and the outline of future steps to take in this project.

4.1 Discussion of Experiment Results

By varying the distance from the target to the detector, we observe that there is a possible field divergence as the distance increases. To observe this, multiple scans were created, ensuring to keep the same orientation of the detector at varying distances.

One particular set of scans was used to estimate the deflection angle of the beam. For this set of scans, the detector was placed 6 and 8 centimeters from the target, and the program to execute the scans was set to move through a region of 2.54×2.54 cm, which corresponds to a 40×40 grid in the program.

After analyzing the various scans, the divergence angle was computed thus: let h be the deviation of the peaks from the lateral position, and α the angle of divergence. Then from the above, with the distance between the two detector positions 20 mm, we have the relationship

$$\tan \alpha = \frac{h}{20}.$$

The true peak locations were found to deviate by $h = 0.53975$ mm. From this, we found the angle of deviation from the center line was $\alpha = 1.5459^\circ$, so the angle of divergence is 3.0918°. This information gives some preliminary results on fabricating an acoustic lens with acrylic. The scans used to determine this information are displayed in figures 4.1, 4.2, and 4.3.

The proposed acoustic lens is to have a plano-concave shape, with one side flat. We use the

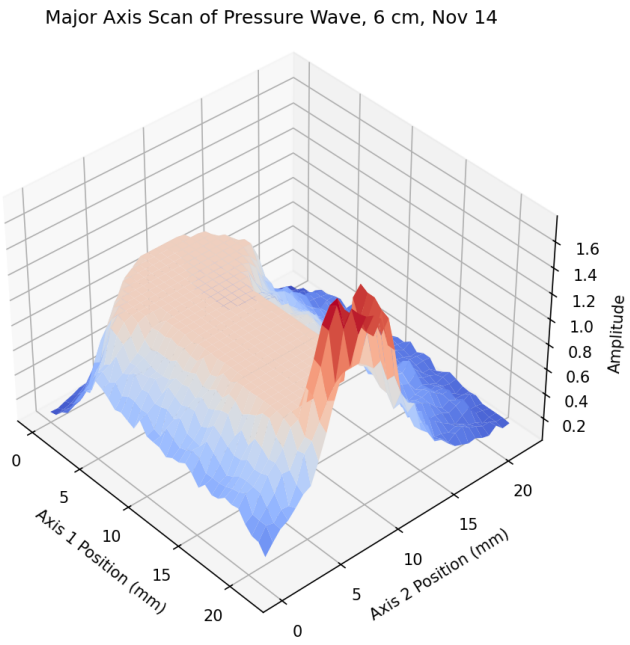

Figure 4.1: A surface plot of an ultrasound pressure wave as measured 6 centimeters from the target. The spike at the "bottom" of the plot is a possible reflection from the glass in the tank.

lens-makers' formula for this case, as found in [12]:

$$\frac{1}{f} = (n-1)\frac{1}{R}$$

where f is the focal length of the lens, n is the refractive index, and R is the radius of curvature of the convex side. To determine the refractive index n, we must compare the speed of sound in water, which is 1500 m/s and in acrylic, which is 2730 m/s. The refractive index is thus

$$n = \frac{2730}{1500} = 1.82.$$

Now, using this in the lens-makers' formula stated previously, in order to achieve a focal length of 8 cm, the concave side of the lens should have a radius of curvature $R = 65.6$ mm. This radius of curvature is then used to compute the depth of a cut in an acrylic rod of diameter 1.5 in. Through a geometric argument, it can be shown that the required cut depth is 2.83 mm.

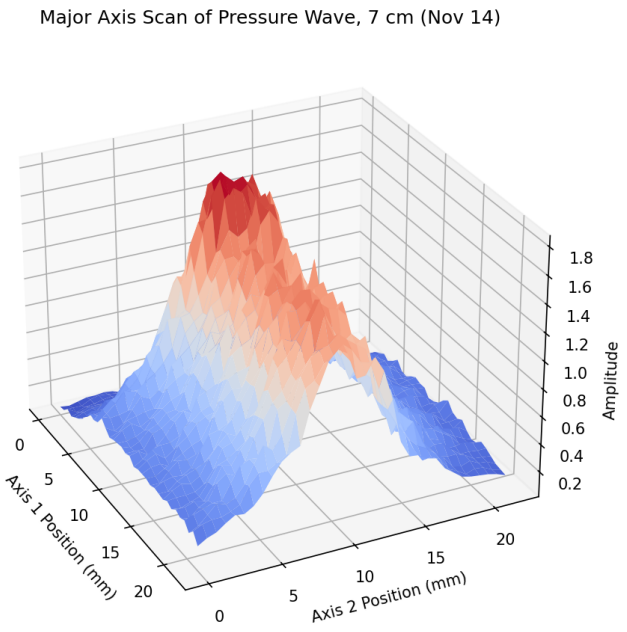

Figure 4.2: A surface plot of an ultrasound pressure wave as measured 7 centimeters from the target. Note the peak is less flat as in figure 4.1.

4.2 Challenges and Future Work

Throughout the project, there were several challenges to overcome. Despite these obstacles, the project did progress through the term, and a blueprint for continued work was created.

One of the primary challenges was the interfacing of the present hardware with the LabView graphical programming environment. Unlike traditional programming languages, LabView uses wire diagrams, similar to MathWorks' Simulink, to execute routines. The modules created in the LabView environment can be interfaced with physical hardware, allowing the user to display information in a Virtual Instrument (VI) on the screen. The VI also contains controls for user input and output, allowing for custom applications to be created. However, the way in which these VIs are created is cumbersome, requiring wiring of various modules with few methods of organizing the block diagram within a window. Nonetheless, the versatility of LabView allowed for easy processing of data from hardware, thereby making the data collection process relatively straightforward.

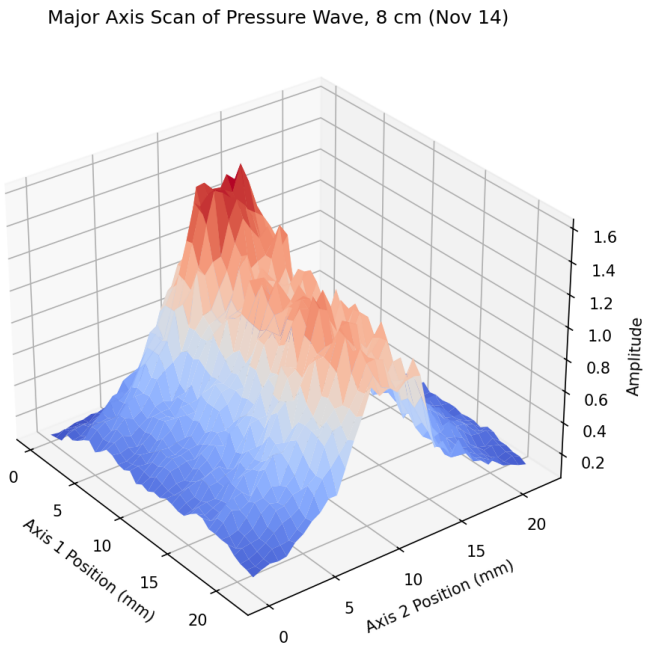

Figure 4.3: A surface plot of an ultrasound pressure wave as measured 8 centimeters from the target. The peak height also shows decay, as expected.

The detector setup, as seen in figure 3.2, did pose some problems during the experiments. When calibrating for a scan, the angle of the detector affected the quality of the signal collected by the oscilloscope. In each new set of scans, care was taken to ensure that the detector was placed at the same distance from the detector and that its orientation was consistent. At first, the detector was aligned so that it was parallel to the posts mounted on the translation stage motors, but this did not produce the optimal output. This may be changed in a new detector design, as the present one is a prototype for preliminary experiments.

Future work for the project consists of two parts. First, after the acoustic lens is created, new scans of the response field will be made to determine if the field is focused. If needed, different lenses may be fabricated with varying focal lengths and shapes to determine the best combination for the imaging application. We will also compare the field's shape through a varying aperture width to examine if truncating the beam profile to be more circular will provide a significant difference. Second, we will image the test material, as seen in figure 4.4. The objective is to detect the

phantoms in a reconstructed image. A previous experiment conducted before this current project resulted in a successfully reconstructed image of the material, but the phantoms appear elongated. In figure 4.5, the bright red areas of the reconstructed image are intended to represent the various defects of the phantoms, but the combination of the beam shape, reflection of the beam from the material edge, and diverging field cause the smearing effect. Designing an image reconstruction algorithm to minimize this effect in the output will be a primary task, along with ensuring sufficient resolution of the scans to provide a meaningful result.

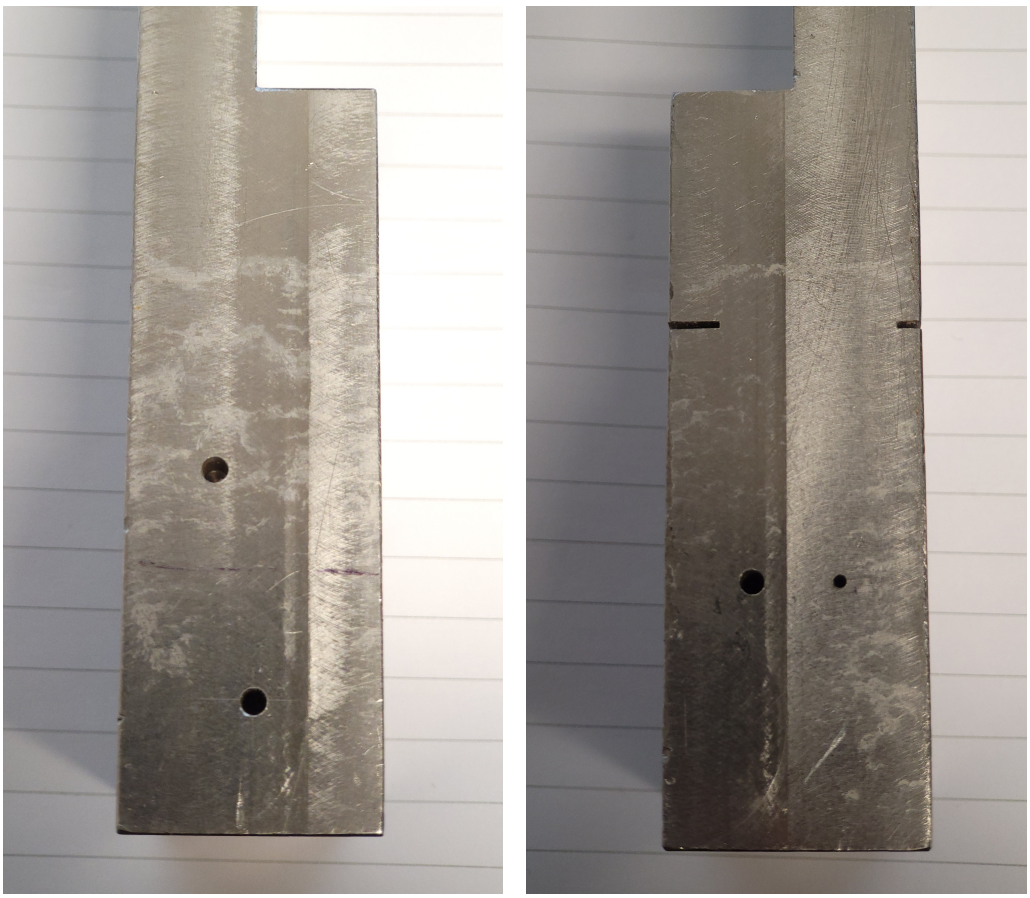

Figure 4.4: The material to be imaged, with the circular phantoms.

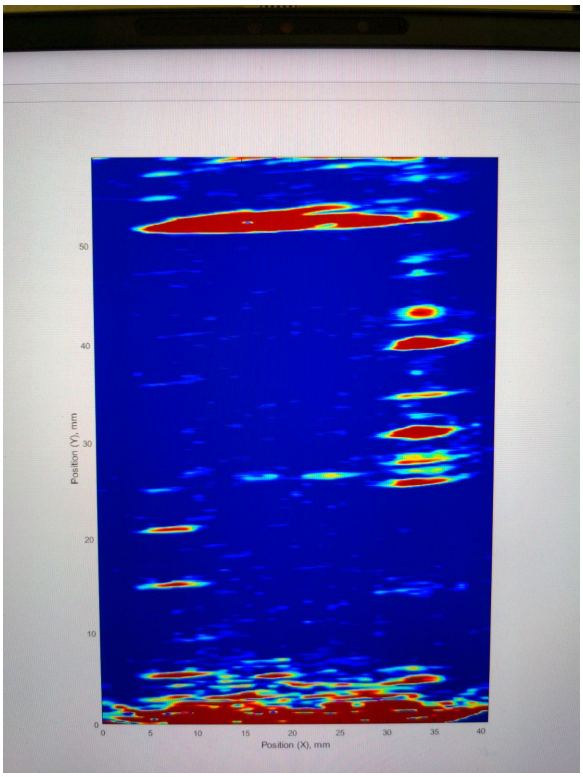

Figure 4.5: A photograph of previous experiment results showing the elongated phantoms.

4.3 Conclusions

The present experiments demonstrate some of the basic properties of the acoustic field in our application. After examining its properties, we have identified that the field diverges and affects the imaging of a material. Despite this shortcoming, the principles of photoacoustic sensing related to imaging are rooted in the second-order wave equation. The main goal is to determine a source function based on the signals acquired. The imaging problem, which is an inverse problem, is difficult, but good approximations can be found by various techniques. Work is needed to improve the imaging methods, including the development of rudimentary reconstruction and phantom detection algorithms, which could be phased into a larger set of projects.

The imaging of materials is useful in both medical and industrial applications, especially in the detection of defects. Care must be taken to design an imaging process that captures the characteristics of the phantoms and is not computationally expensive on conventional hardware. Such

an algorithm would need to be tested and refined over many sessions, and a machine learning approach would need to have its parameters tuned carefully to optimally image the material and best represent the phantoms. After a procedure is designed and implemented, next steps can be taken to integrate the techniques in large-scale industrial settings.

This project served to meet several educational and professional goals. The Applied-Industrial Mathematics degree program at UTSA aims to give its students the skills to do mathematics in an industrial setting, with an emphasis on applications in the sciences and beyond. Gaining experience conducting research in the growing field of photoacoustics meets the goals of the program, preparing a student for a career as a research scientist.

REFERENCES

[1] Lokenath Debnath. *Integral Transforms and Their Applications*. Chapman and Hall/CRC, Boca Raton, Fla. [u.a.], 2nd edition, 2007. Includes bibliographical references and index. - Previous ed.: 1995.

[2] Charles L. Epstein. *Introduction to the mathematics of medical imaging*. Pearson [u.a.], Upper Saddle River, NJ, 2003.

[3] Lawrence C. Evans. *Partial Differential Equations*. Number 19 in Graduate studies in mathematics. American Mathematical Society, Providence, Rhode Island, second edition, 2022. Literaturverzeichnis: Seite 689-701. - Index.

[4] Timothy G. Feeman. *The Mathematics of Medical Imaging*. SpringerLink. Springer, Cham, 2nd ed. 2015 edition, 2015.

[5] Randolph D. Glickman. Photoacoustic imaging and sensing: A new way to see the eye. *Journal of Ocular Pharmacology and Therapeutics*, 37(3):162–171, April 2021.

[6] Markus Haltmeier, Stephan Antholzer, Johannes Schwab, and Robert Nuster. Photoacoustic image reconstruction via deep learning. In Alexander A. Oraevsky and Lihong V. Wang, editors, *Photons Plus Ultrasound: Imaging and Sensing 2018*. SPIE, February 2018.

[7] Dan Hill. How to convert FWHM measurements to $1/(e^2)$ halfwidths, March 2021.

[8] Steven L. Jacques. Laser-tissue interactions. In Kenneth Hardy, Martin L. Meltz, and Randolph Glickman, editors, *Non-Ionizing Radiation: An Overview of the Physics and Biology*, chapter 6. Health Physics Society, Madison, WI, 1997.

[9] L. Li. Photoacoustic imaging. *Pathobiology of Human Disease*, pages 3912–3924, 2014.

[10] Saher M. Maswadi et al. All-optical optoacoustic microscopy based on probe beam deflection technique. *Photoacoustics*, 4(3):91–101, September 2016.

[11] G Paltauf, R Nuster, M Haltmeier, and P Burgholzer. Experimental evaluation of reconstruction algorithms for limited view photoacoustic tomography with line detectors. *Inverse Problems*, 23(6):S81–S94, November 2007.

[12] Raymond A. Serway and John W. Jewett. *Physics for Scientists and Engineers with Modern Physics*. Cengage Learning, 7 edition, 2008.

[13] Gilbert Strang. *Linear Algebra and Learning from Data*. Wellesley - Cambridge Press, Wellesley, MA, 2019. Literaturverzeichnis: Seite 416.

[14] Walter A. Strauss. *Partial Differential Equations*. Wiley, Hoboken, NJ, 2. ed. edition, 2008. Previous ed.: s.l.: Wiley, 1992.

APPENDIX A

ECHOLASE, INC. CONTACT INFORMATION

Echolase, Inc. is a startup based in San Antonio, Texas headed by Dr. Saher Maswadi (maswadi@echolase.com) and Dr. Randolph Glickman (glickman@echolase.com, 210-289-2935). The office is located at 4335 Vance Jackson Rd, Suite 203, San Antonio, TX 78230.

APPENDIX B

GITHUB REPOSITORY

All relevant data, code, and graphics generated are hosted on GitHub at `https://github.com/SZRoberson/EcholaseAIM`. The data collected is hosted on Google Drive, with the link in the GitHub repository inside the file `README.md`.